

POLARIMETRIC ANALYSIS OF ALOS PALSAR DATA (POL-SAR) OVER TEST AREAS IN NORTH-WEST BULGARIA — POLARIMETRIC DESCRIPTORS, DECOMPOSITIONS AND CLASSIFICATIONS

Zlatomir Dimitrov

*Space Research and Technology Institute — Bulgarian Academy of Sciences
e-mail: zlatomir.dimitrov@space.bas.bg*

Keywords: *POL-SAR, Polarimetry, ALOS1 PALSAR, Polarimetric coherences, Polarimetric decompositions*

Abstract

This study is focused on utilizing full-polarimetric L-band radar data from ALOS PALSAR (JAXA) by means of Polarimetry (POL-SAR), over mountainous test sites in Bulgaria. General aim is to show feasibility of the Polarimetry to describe natural targets, which exhibits various scattering mechanisms in respect to their bio-physical and geometrical properties. Firstly, the importance of Covariance and Coherent matrices is shown which is followed by calculation of the polarimetric coherences with their particular significance. The mathematical and physical model based decompositions are applied to describe backscattering media from scattering mechanisms. Radar indices resulted from H/A/ α -decomposition showed randomization of scattering mechanisms over forest areas, whilst two major scattering mechanisms are observed mainly in crop lands. A comparison is made between polarimetric descriptors from acquisitions in different seasonality over mountainous forest and agricultural lands. Polarimetric segmentations and classifications are applied, with 8 (H/A) and 16 (H/A/ α) components. Finally, a forest mask is proposed based on relevant polarimetric descriptors. Study showed good utilization and importance of the full-polarimetric L-band SAR data, derived from ALOS PALSAR, in natural targets and forest areas. This report resulted from a course GEO414 — “Polarimetrie” held at the University of Jena, Lehrstuhl für Fernerkundung, in the framework of ERASMUS+, with the kind support of — Dr. T. Jagdhuber (DLR) and Prof. C. Schmullius.

Introduction

Radar polarimetry (POL-SAR) is essential technique in polarimetric SAR analysis exploiting relation of polarization states to the geometrical properties and physical state of the scattering objects within scattering media [1]. The type of polarimetric content from dual- or quad-polarimetric datasets is essential for the accuracy of natural media classifications [2]. The Advanced Land Observing Satellite (ALOS) is Japan’s most successful full-polarimetric EO satellite by its Phased Array L-band SAR (PALSAR) instrument launched in 2006 [3]. Due to better sensitivity of L-band to the vegetation, moreover by means of polarimetry at

the forest volume, PALSAR is preferable instrument for forest structure information extraction [1, 4]. To link SAR observables with structure of the scattering media, target decomposition theory is introduced where modeling the backscatter with certain reflection symmetry is derived [5]. Benefits of model based approach for scattering power decomposition gives better understanding of volume backscatter and discrimination of vegetation from oriented urban areas using PALSAR PLR data [6]. Thus, an advanced approaches for modeling depolarization of soil-trunk double bounce scattering are proposed focusing on extended Fresnel scattering [7].

In this study general application of Polarimetry (POL-SAR) is considered with emphasis on natural targets. Utilization of ALOS1-PALSAR full-pol SAR data is made in mountainous and flat area with variety of land cover. Outcomes of the polarimetric coherences over natural scattering media is considered. Accent is given on decomposition theorems such as Eigen-based ($H/A/\alpha$) and physical model based (Yamaguchi-3, Freeman-2) including variety of polarimetric descriptors and radar indices (e.g. RVI). Polarimetric segmentations and classifications are involved where, finally, a Forest/Non-forest mask is proposed. Processing and analysis of PALSAR scenes is performed within PolSARPro v.5 (software by IETR, Prof. E. Pottier) without geocoding in Radar geometry. Geocoding is made in ESA-SNAP.

This report is resulted from the Master course — GEO414 “Polarimetric”, held at the University of Jena (FSU-Jena), Lehrstuhl für Fernerkundung, with the kind support of lecturer Dr. Thomas Jagdhuber and Prof. Christiane Schmillius.

The report was also presented in Bulgarian on the Seventeenth International Scientific Conference “Space, Ecology, Safety” — SES 2021, Sofia, 20–22 October 2021, held online, at Space Research and Technology Institute — BAS.

Polarimetry basics

The formulation of POL-SAR begins with the Maxwell’s laws for electromagnetic waves crossing over the Stokes parameters. General statement of the Jones vector formalism considers the important property of the Electric vector orientation in space [5]. The polarization ellipse of the Electric vector defines general property in polarimetry, namely — *linear*, *circular* and *elliptical* polarization states [8]. Hence, the polarimetric states of the emitted and received chirp is formulated as a Scattering (Sinclair’s) matrix considering linear basis (H, V) where:

$$(1) \quad [S] = \begin{bmatrix} S_{hh} & S_{hv} \\ S_{vh} & S_{vv} \end{bmatrix}$$

In general, polarimetric theory assumes *reciprocity* that considers equilibrium of the cross-pols — $S_{hv} = S_{vh}$. Physical process of the backscatter considers two types of scattering targets — deterministic (or coherent) and non-deterministic (or natural/distributed). Considering the point target vector, *coherent targets* are point scatterers, the amplitude of the point target vector holds most of the backscattered energy; whereas, at the *natural targets* — backscattered energy is

distributed over individual backscatterers thus vector sum is random [5]. Therefore, describing scattering process from natural media in the case of reciprocity, the Second order statistics is defined in terms of two rang-3 Hermitian matrices [8] such as:

- Covariance Matrix — $[C_3]$

$$(2) \quad \overrightarrow{k_{3L}} = (S_{HH} \quad \sqrt{2}S_{XX} \quad S_{VV})^T \rightarrow [C] = \langle \overrightarrow{k_{3L}} \cdot \overrightarrow{k_{3L}}^* \rangle = \begin{bmatrix} C_{11} & C_{12} & C_{13} \\ C_{21}^* & C_{22} & C_{23} \\ C_{31}^* & C_{32}^* & C_{33} \end{bmatrix} =$$

$$\begin{bmatrix} |S_{HH}|^2 & \sqrt{2}S_{HH}S_{XX}^* & S_{HH}S_{VV}^* \\ \sqrt{2}S_{HH}^*S_{XX} & 2|S_{XX}|^2 & \sqrt{2}S_{XX}S_{VV}^* \\ S_{HH}^*S_{VV} & \sqrt{2}S_{XX}^*S_{VV} & |S_{VV}|^2 \end{bmatrix},$$

where: $S_{XX} = S_{HV} = S_{VH}$ is cross – polarized scattering for monostatic systems.

- Coherence Matrix — $[T_3]$:

$$(3) \quad \overrightarrow{k_{3P}} = \frac{1}{\sqrt{2}}(S_{HH} + S_{VV} \quad S_{HH} - S_{VV} \quad S_{HV} + S_{VH})^T \rightarrow [T] = \langle \overrightarrow{k_{3P}} \cdot \overrightarrow{k_{3P}}^* \rangle = \begin{bmatrix} T_{11} & T_{12} & T_{13} \\ T_{21}^* & T_{22} & T_{23} \\ T_{31}^* & T_{32}^* & T_{33} \end{bmatrix}$$

$$= \frac{1}{2} \begin{bmatrix} |S_{HH} + S_{VV}|^2 & (S_{HH} + S_{VV})(S_{HH} - S_{VV})^* & 2(S_{HH} + S_{VV})S_{XX}^* \\ (S_{HH} + S_{VV})^*(S_{HH} - S_{VV}) & |S_{HH} - S_{VV}|^2 & 2(S_{HH} - S_{VV})S_{XX}^* \\ 2(S_{HH} + S_{VV})^*S_{XX} & 2(S_{HH} - S_{VV})^*S_{XX} & 4|S_{XX}|^2 \end{bmatrix}$$




Important is to be stated, that the $[T_3]$ and $[C_3]$ are derived from Pauli and Lexicographic target vectors respectively. Those matrices are the starting point for polarimetric analysis in natural media, in order to describe depolarization.

Study area and polarimetric SAR data

In this survey, polarimetric SAR data from ALOS-1 PALSAR (JAXA) — PLR datasets are used, provided via PI proposal from ESA Third Party mission. The test area (AOI) is selected according to the test sites from the Author's PhD study, located in the North-West Bulgaria, along Stara Planina mountain massif and the Danube River valley. It comprises forest areas in rugged terrain with steep slopes, also characterized with many agricultural lands with crop types for the time of acquisitions — maize, corn, and sunflower. Rural areas are small, neighboring with reservoirs and standing water bodies. Many grasslands are also common in the forest areas.

Table 1. Scene parameters of ALOS PALSAR –full polarimetric (PLR) SAR data acquisition parameters, over selected test sites

PARAMETERS	SCENE - 1	SCENE - 2	SCENE - 3
Date of acquisition	2007-05-10	2007-11-10	2009-05-15
Product type	PLR_SLC_1P	PLR_SLC_1P	PLR_SLC_1P
Orbit	Ascending	Ascending	Ascending

Polarimetric channels	HH, HV, VH, VV	HH, HV, VH, VV	HH, HV, VH, VV
Azimuth Res.	3.57063 [m]	4.03544 [m]	4.03577 [m]
Range Res.	9.36852 [m]	9.47558 [m]	9.47558 [m]
Incidence angle	23.937 [deg]	23.944 [deg]	25.764 [deg]
Lines	1 344	1 344	1 216
Rows	24 320	24 512	22 528
Type and format	Level 1.1 / CEOS	Level 1.1 / CEOS	Level 1.1/CEOS
Test site in PhD	TS20	TS20	TS21
Comment over the selected chip	Forest area and a bit of agricultures.	Forest area and a bit of agricultures.	Large agricultural diversity, forests.
Meteo situation in the time of acquisition	In Spring; Clear and calm weather, no rain. T.16°C; Hum.59%.	Cold Autumn, wind and rain; Severe weather. T.3°C; Hum. 69%.	Warm Spring, with precipitation. Calm and wet weather. T.20°C; Hum. 78%.
Referent MODIS imagery in the day of acquisition			

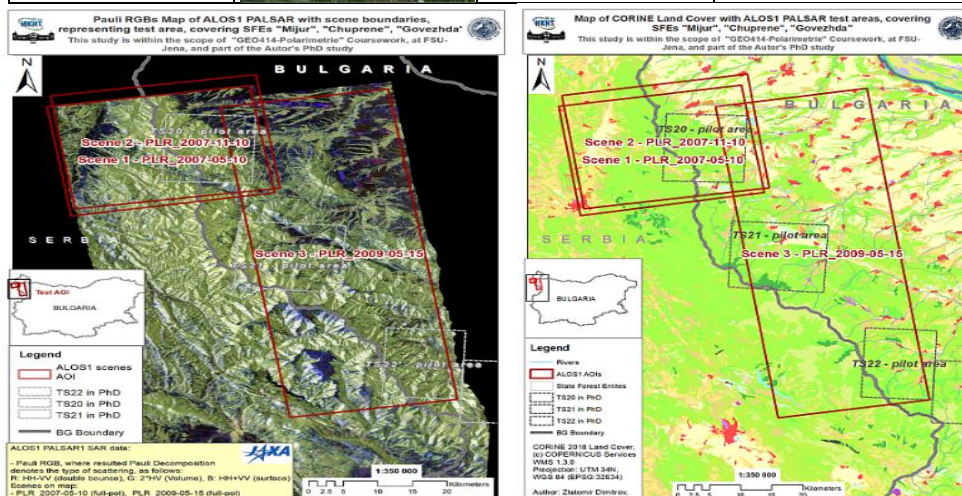


Fig 1. Test sites boundaries, resulted from ALOS1 scenes footprint are presented, over two Pauli-Basis (RGB) from two PALSAR acquisitions (left), over CORINE land cover (right). The test sites boundaries from Author's PhD study are also pictured, in greyish dashed.

Polarimetric Methods Applied and Results

Analysis via single matrix elements

On first instance analysis is made via Sinclair's elements from scattering matrix $[S_2]$, valid for coherent targets only [5]. Testing correlation of the matrix

elements in between showed low correlation at S_{11} vs. S_{12} , correlation at S_{11} vs. S_{22} , and best correlation between S_{12} vs. S_{21} which is true for monostatic systems.

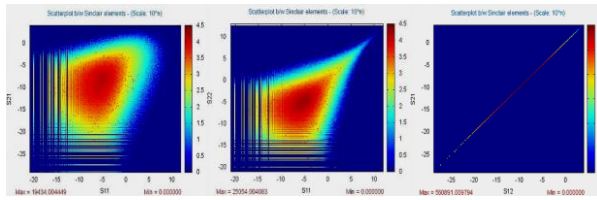


Fig. 2. Correlative plots between Sinclair's elements of $[S]$; from left to right: $S_{21}\sim S_{11}$, $S_{22}\sim S_{11}$, $S_{21}\sim S_{12}$

The on-screen analysis between Scene-1 and 2 showed general difference within normalized radar cross-section, in-between the co-pol and cross-pol channels of $[S_2]$ mainly over non-forest area. Geometric distortions — foreshortening in mountainous forest gives high backscatter, with differences more than 5 dB. Highest backscatter difference is observed over agricultural lands where some of the crops produces high backscatter toward sensor in Sinclair's elements with polarizations HH and VV; whilst, the HV & VH decreased with more than 20 dB (see Fig. 3).

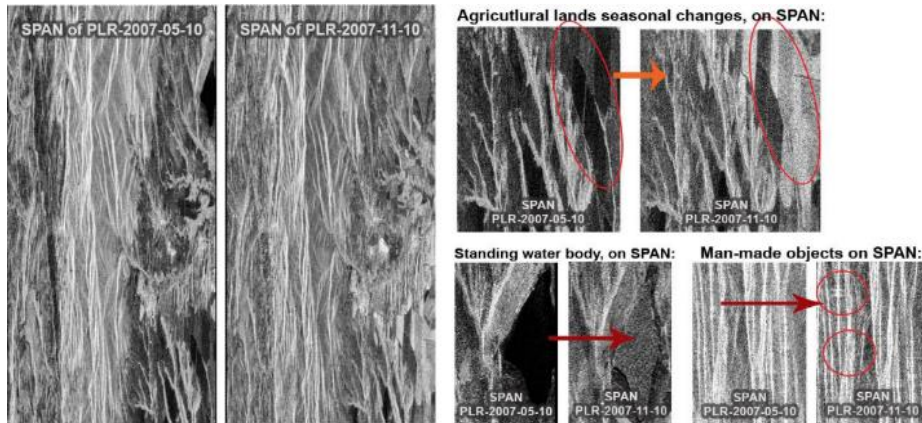


Fig. 3. Total backscattered power — SPAN of scattering matrix $[S]$, comparison between Scene — 1 and 2 in two different areas of land cover types that exhibits differences in the backscatter power, registered by the sensor (©ESA/JAXA – PALSAR)

The analysis by means of SPAN — representing the total backscattered power, revealed lower backscatter in forest areas, because of the leaf-off in forest. Over the standing water body in November's scene a strong backscatter toward sensor is observed, which points out a rough surface, possibly caused by a rainfall.

Direct interpretation of $[C_3]$ and $[T_3]$ matrix elements showed following dependencies in vegetation (see Fig. 4): registered backscatter intensity on C_{11} representing HH-polarization is equal with the T_{11} ; more than 19 dB is observed

between C_{11} and C_{22} , representing Volume backscatter. Above 10 dB difference is observed between C_{22} and T_{22} , and C_{22} and T_{33} over distributed targets, although the calculated total power in SPAN is very high (ab. 0 dB). That leads to strong backscatter toward sensor, from natural targets. The C_{33} representing VV polarization in common cases is higher than C_{11} over distributed targets.

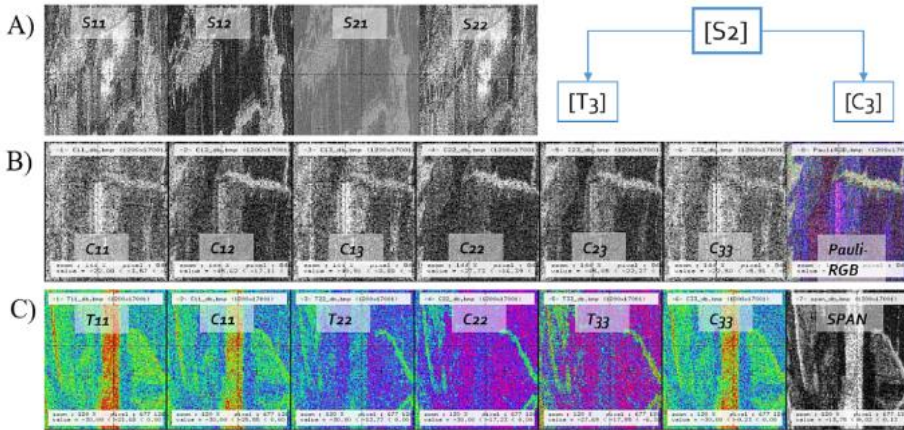


Fig. 4. Matrix elements representation over agriculture — A) Sinclair's (Scattering Matrix) elements; B) Second order statistics of Covariance matrix elements, with Pauli-Basis; C) Second order statistics of Coherence matrix elements, with SPAN (©ESA/JAXA – PALSAR)

Analyzing urban areas, where the degree of depolarization is very low, high backscatter is observed with almost equal intensity of T_{11} , C_{11} T_{22} , but lower in C_{33} .

Therefore, considering the $[T_3]$ and $[C_3]$ matrix elements, it could be concluded that Coherency matrix is preferable in Polarimetric analysis of non-deterministic (distributed) targets, due to its direct interpretation of scattering mechanisms. In spite, usage of Covariance matrix should be prompt, when aiming the direct interpretation of the polarimetric channels information.

Polarimetric speckle filtering

In polarimetric analyses speckle filtering is essential in order to reduce the ambiguities between systematical noise and useful information. In general case it is some kind of tradeoff between spatial accuracy and characteristic noise suppression [8]. Variety of polarimetric filtering techniques exists, where the mono-temporal non-adaptive/adaptive polarimetric speckle filters are related to the spatial domain, where incoherent averaging is performed to the $[T_3]$ and $[C_3]$ [9].

To test polarimetric speckle filtering over the PALSAR polarimetric imageries, two type of filters are used: BOXCAR and Refined Lee. Result is presented in Fig. 5, where different size of averaging windows is used, over coherent and non-coherent targets [9].

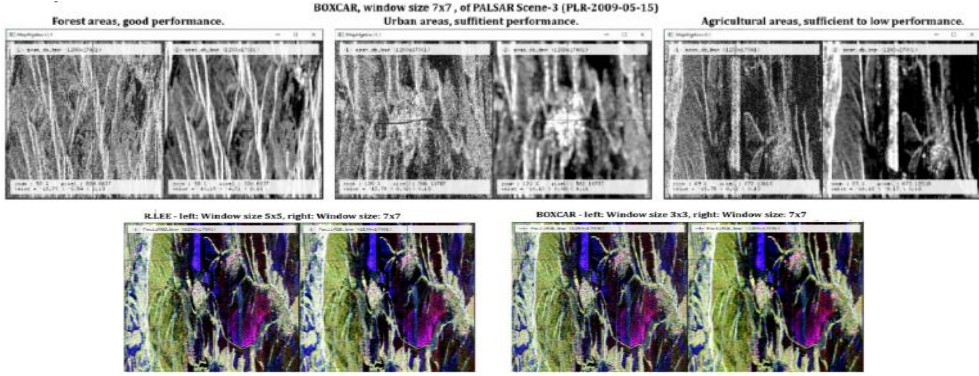


Fig. 5. Speckle filters BOXCAR and R. Lee — applied over coherent and non-coherent targets, using SPAN and Pauli-Basis (Pauli-RGB) of Scene-3, with different windows

Window sizes of 5×5 or 7×7 are found to be reasonable over natural targets.

Polarimetric coherences — analysis in HH , VV and LL , RR basis

Polarimetric coherences are complex correlation coefficients between off-diagonal complex Hermitian matrices elements, with indexes — H_{12} , H_{13} , H_{23} where “H” is element from $[T_3]$ or $[C_3]$. Correlation coefficients could be calculated either in Linear (HH , VV) or in Circular (LL , RR) basis [8]. Formulation of the correlation coefficients for natural targets, tested in the study, is:

$$(5) \quad \gamma_{HH \pm VV} = \gamma_{T12} = Ro12 = \frac{\langle T_{12} \rangle}{\sqrt{\langle T_{11} \rangle \langle T_{22} \rangle}} = \frac{\langle (S_{hh} + S_{vv})(S_{hh} - S_{vv})^* \rangle}{\sqrt{\langle |S_{hh} + S_{vv}|^2 \rangle \langle |S_{hh} - S_{vv}|^2 \rangle}}$$

$$(6) \quad \gamma_{(HH+VV)HV} = \gamma_{T13} = Ro13 = \frac{\langle T_{13} \rangle}{\sqrt{\langle T_{11} \rangle \langle T_{33} \rangle}} = \frac{\langle 2(S_{hh} + S_{vv})S_{xx}^* \rangle}{\sqrt{\langle |S_{hh} + S_{vv}|^2 \rangle \langle 4|S_{xx}|^2 \rangle}}$$

$$(7) \quad \gamma_{(HH-VV)HV} = \gamma_{T23} = Ro23 = \frac{\langle T_{23} \rangle}{\sqrt{\langle T_{22} \rangle \langle T_{33} \rangle}} = \frac{\langle 2(S_{hh} - S_{vv})S_{xx}^* \rangle}{\sqrt{\langle |S_{hh} - S_{vv}|^2 \rangle \langle 4|S_{xx}|^2 \rangle}}$$

$$(8) \quad \gamma_{HHVV} = \gamma_{C13} = Ro13 = \frac{\langle C_{13} \rangle}{\sqrt{\langle C_{11} \rangle \langle C_{33} \rangle}} = \langle S_{hh} S_{vv}^* \rangle / \sqrt{\langle |S_{hh}|^2 \rangle \langle |S_{vv}|^2 \rangle}$$

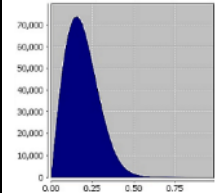
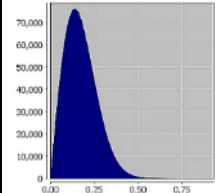
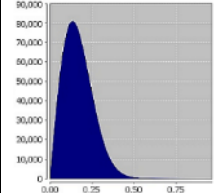
$$(9) \quad \gamma_{RRLL} = \gamma_{CCC} = C.C.C. \text{ and } |C.C.C.| = \frac{\langle C_{lr} \rangle}{\sqrt{\langle C_{ll} \rangle \langle C_{rr} \rangle}} = \frac{\langle S_{ll} S_{rr}^* \rangle}{\sqrt{\langle |S_{ll}|^2 \rangle \langle |S_{rr}|^2 \rangle}}$$

Correlation coefficients are calculated with size of the averaging window — 7×7 , for whole PALSAR — PLR data.

Analysis of Ro12, Ro13 and Ro23, derived from $[T_3]$:

Statistics have been calculated, showing mean value of coherences ab. 0.16, pointing out low coherence between particular scattering mechanisms; see table.

Table 2. Statistics and distribution of the Correlation coefficients based on [T3], of Scene-3

Modulus of:	Ro12 (γ_{HH+VV})	Ro13 ($\gamma_{(HH+VV)HV}$)	Ro23 ($\gamma_{(HH-VV)HV}$)
Max	0.9633	0.8844	0.9165
Mean	0.1806	0.1548	0.1604
Median	0.1713	0.1557	0.1521
Histograms			

Highest correlation at the modulus of the correlation coefficients is found over agricultural areas, where the phase shows better consistency than the modulus, with good object's delineation. From the three coherences, the **Ro12**(γ_{T12}) — shows the best polarimetric correlation, with modulus of ab. 0.67–0.81 over crops (Fig. 6).

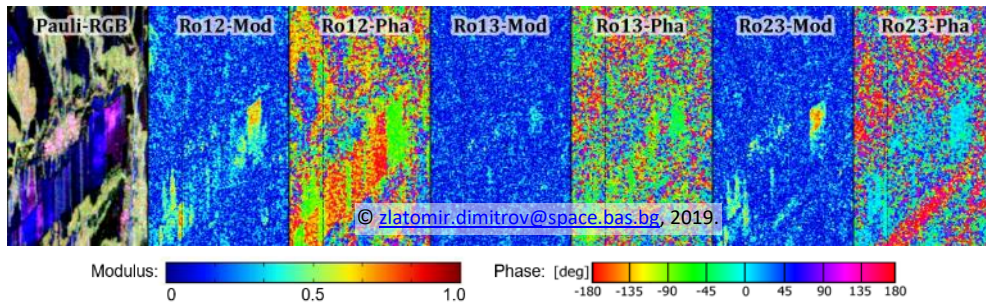


Fig. 6. Polarimetric correlation coefficients, derived from — [T3]: Ro12, Ro13 and Ro23 with Pauli Decomposition (©ESA/JAXA – PALSAR)

In forest and urban areas low coherence is observed. Phase is showing good consistency and distinct landcover objects are recognizable. In sparse or non-forest areas, angle between scattering mechanisms is: -90 deg (yellowish in Fig. 6). Over agricultural areas the phase angle is homogenous (green and red), where crops could be delineated. Over forest areas, phase keep random values. The **Ro23**(γ_{T23}) also shows good polarimetric correlation over some distinct agricultural areas, with modulus of 0.5. Phase of Ro23 suggests changes in forest structure over flat forest with values of -170 deg (reddish in Fig. 6). Phase over neighboring agriculture varies from -45 to 45 deg (bluish in Fig. 6). Interestingly, the **Ro13**(γ_{T13}) in general is noisy, except at the high mountain. There, phase angle delineates very well grassland from forest, with values below 130 deg; modulus shows less consistency (see Fig.7).

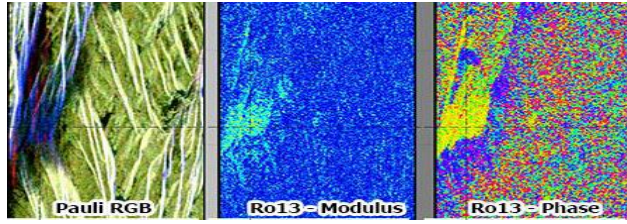


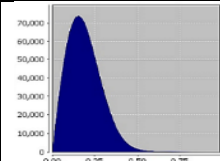
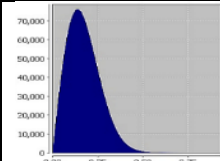
Fig. 7. Top hill area in the mountains on Scene-3, which exhibits surface scattering. This is the only area where the modulus of Ro13 is showing values ab. 0.6. In spite, grassland could be easily delineated from forest. (©ESA/JAXA – PALSAR).

Interpretation of the complex polarimetric coherences derived from $[T_3]$, should reveal the apposition of scattering mechanisms within the scattering media. Higher modulus (amplitude) of polarimetric coherence means equal input of those scattering mechanisms. Phase angle suggests the height of the scattering phase centers — e.g. vertical location of canonical scattering mechanisms. Hence, the high values of Ro12 (γ_{T12}) should express equal contribution of the Dihedral and Surface scattering. Over natural media such as forests, input of scattering mechanisms is highly varying, thus modulus trends to zero; phase angle is random, which suggests different height of the canonical scattering mechanisms. The top-hill area where Ro13 (γ_{T13}) modulus is high is due to presence of surface scattering.

Analysis of Ro13, C.C.C and Normalized C.C.C, derived from $[C_3]$:

Contrariwise, the polarimetric coherences derived from $[C_3]$ are showing higher correlation, whilst the Ro13 (γ_{C13}) shows highest mean correlation at all.

Table 3. Statistics and distribution of the Correlation coefficients based on $[C_3]$, of Scene-3

Modulus of:	Ro13 (γ_{HHVV})	C.C.C (γ_{LLRR})
Max	0.9971	0.9363
Mean	0.4261	0.1806
Median	0.4118	0.1713
Histograms		

The **Ro13(γ_{HHVV})** derived from $[C_3]$ allows direct interpretation on polarization result from correlation of HH vs. VV at target vector. Considering the Ro13 (γ_{HHVV}), highest coherence is observed over deforested areas in the mountains, or over crops where values in the modulus reaches up to 0.98! Thus, those areas are very well recognizable. Thus, phase of Ro13 (γ_{HHVV}) is circulating around zero degrees, with exception over natural media. Over forest modulus drops, showing no correlation. Considering the modulus of the polarimetric coherence in circular

basis — LL,RR , shows high correlation at non-forest areas — especially agriculture where values are ab. 0.84, despite very low values over forest areas. The phase of the Circular Correlation Coefficient (C.C.C.) there, is much more consistent with homogenous trend about 180 deg, over grassland and crops. The Normalized C.C.C. showed exactly the opposite trend in modulus — high values over forest areas.

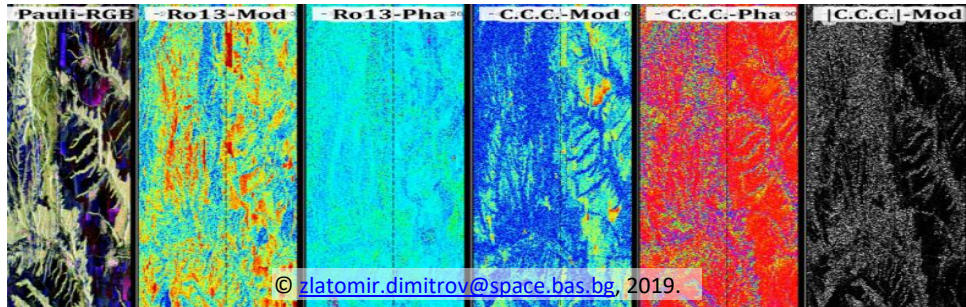


Fig. 8. Polarimetric coherences derived from Coherency matrix, Scene-3 (©ESA/JAXA – PALSAR)

Considering direct **interpretation**, the Ro13 (γ_{HHVV}) shows high correlation over areas with surface scattering, e.g. grasslands and agriculture. In such scattering media, energy loss is not so much, thus the depolarization is less and phase angle between HH and VV vectors stays almost constant. This is not the case in forest areas where volume scattering is accompanied by strong depolarization and energy loss. Interestingly, switching into LL,RR basis the C.C.C. (γ_{LLRR}) delineates very well forest from non-forest area, which is a result from helix backscatter in the media.

Polarimetric Decompositions — mathematical and physical based

Polarimetric decompositions express the measured backscattered signal in scattering matrix, as a sum of particular responses of simple canonical objects [5]. Considering coherent deterministic targets, a coherent decomposition theorems exists, such as Pauli, Kroager, via Scattering matrix. Considering non-deterministic targets, where complete depolarization is observed, the incoherent decompositions are applied via Hermitian matrices. Those decomposition theorems are based either on physical model such as Freeman-Durden, Van-Zyl or based on mathematical based approach such as Eigen-based — H/A/alpha. Decomposition theorems are summarized on the diagram below in Fig. 9 [8]. Should be noted that for incoherent decomposition theorems because presence of non-deterministic scatterers averaging is needed according to the coherence test based on Touzi criterion [5].

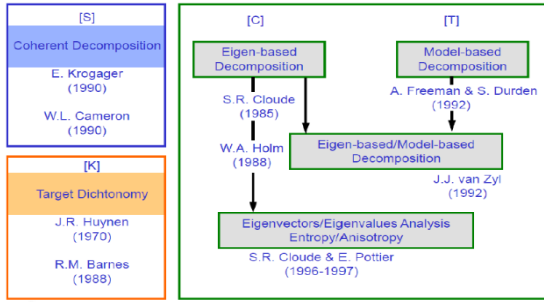


Fig. 9. Summary of Polarimetric Decomposition Theorems [8]

Pauli coherent Decomposition, via [S₂]

The Pauli coherent decomposition theorem is a coherent decomposition theorem, used to describe deterministic targets via [S₂]. It express the measured scattering matrix in the Pauli basis, with the following assumption [10]:

- (10) Dihedral scattering, or Double Bounce: $DB = \frac{1}{2} \langle |S_{HH} - S_{VV}|^2 \rangle$
- (11) Volume scattering, or Dihedral rotated by $-\pi/4$: $VOL = 2 \langle |S_{XX}|^2 \rangle$
- (12) Surface, or odd scattering (Single bounce): $SB = \frac{1}{2} \langle |S_{HH} + S_{VV}|^2 \rangle$

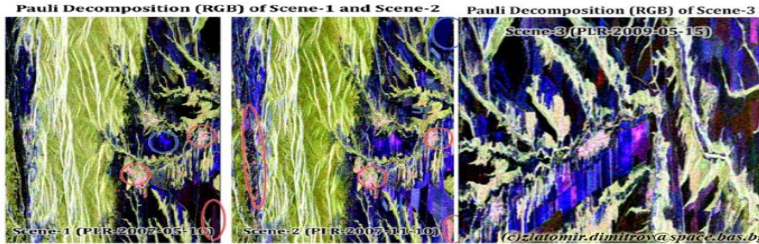


Fig. 10. Pauli coherent Decomposition applied on whole three scenes in different seasonality. In general: Bluish depicts general odd scattering (or Surface), Reddish — even scattering (double bounce), Greenish — multiple scattering (volume). (©ESA/JAXA – PALSAR).

The Pauli decomposition could be related to the Pauli-Basis (Pauli-RGB). The Pauli-coherent decomposition is useful tool in polarimetric analysis because it gives a raw idea over mixture of scattering mechanisms within the backscatter.

From the theorem applied, the following dependencies were observed: at Scene-1 general surface scattering (SB) is observed over crops, bare soils, and some grassland. At Scene-2, and 3, situation is the same with contribution of particular surface scattering from the standing water body due to heavy rainfall at the time of acquisition! The agri-fields was observed to exhibits strong SB and pure DB, for instance from maize or winter crops; some particular agri-fields exhibits bluish to green color, possibly due to mixture of surface and helix scattering. Urban areas in all cases exhibits strong DB mixed with helix scattering (trees nearby). Of course,

non-deterministic scatterers such as forest areas exhibits general volume and helix. Interestingly, during leaf-off period on Scene-2 (due to autumn) more DB scattering could be observed over forest revealing direct backscatter from trunks.

Eigen-based incoherent decomposition — H/A/ α , via [T₃]

Derived from the diagonalization of the Coherency matrix, the Eigen-based decomposition represents [T₃] — as a sum of three individual [T₁] matrices. Those Hermitian matrices are derived from the eigenvectors (u_i) which elements are related to the eigenvalues (λ_i) where: $\infty < \lambda_1 < \lambda_2 < \lambda_3 < 0$ [10] used as Eigenvalues — RGB. Due to the orthogonality, each eigenvalue concerns pure scattering mechanism depicted by α , and orientation around Radar Line Of Sight (RLOS) by β . For interpretation, three well known functions of the eigenvalues are defined related to the physical properties of the scattering media:

$$(13) \text{ Entropy (H): } H = -\sum_{i=1}^3 p_i \log_3(p_i), \quad p - \text{probability: } p_i = \lambda_i / \sum_{k=1}^3 \lambda_k$$

$$(14) \text{ Anisotropy (A): } A = \frac{\lambda_2 - \lambda_3}{\lambda_2 + \lambda_3}$$

$$(15) \text{ Mean_alpha_angle } (\alpha): \bar{\alpha} = \sum_{i=1}^3 p_i \alpha_i$$

Entropy (as in Thermodynamics) is a measure of randomness within the scattering media; **Anisotropy** shows the significance of the second and third scattering mechanisms; **α -angle** controls the change of the scattering mechanisms.

Interpretation of Eigen-based decomposition could be performed either by analyses of H/A/ α or by the eigenvectors-eigenvalues (λ_i) and their pseudo probabilities (p_i) despite all complement to each other [10]. Hence, at Scene-3, the calculated Eigenvalues-**RGB** image is showing equilibrium with the Pauli-decomposition (**RGB**) and consistency with the dominant scattering mechanisms.

Close analysis at the mountainous hilly area (peak “Mijur”, see Fig. 11 — UP) at bluish areas on Eigenvalues-**RGB**, entropy (H) show low values pointing to isotropic surfaces with surface scattering (S). That is confirmed on alpha angle with values close to zero. In that case, the pseudo probability (p_1) shows importance of the first eigenvalue; Anisotropy is low, confirms that only one scattering mechanism contributes to the total power. Interesting situation with a close look over the neighboring **reddish strip** on Eigenvalues-**RGB** shows presence of strong dihedral scattering (D) with high H, A and p_2 ; α — angle points out *isotropic dipole* (*NOT dihedral [10]) with values of 48 deg; β — is homogenous at that area showing small variations around RLOS with ab. 9.8 deg. Contrariwise, at the neighboring **forest area** (greenish on Eigenvalues-**RGB**), H — increases dramatically pointing out complete randomness of the scattering media; α — shows high consistency with this with values near 45 deg pointing to randomly oriented dipoles; β — lies within interval 28–90 deg, showing variations of orientation along RLOS; in forest area — p_1 , p_2 and p_3 show importance of the second and third scattering mechanisms.

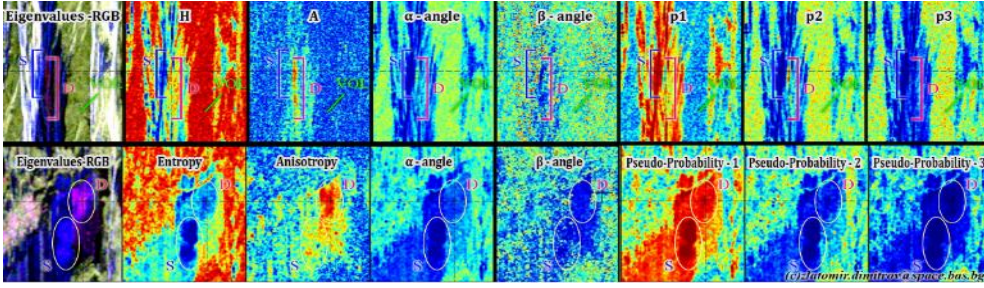


Fig. 11. UP: Hilly area in the mountains near peak “Mijur”, with bare grasslands and forest areas. DOWN: Agricultural area (Agri-area-2) with variety of crops at bottom of Scene-3, with urban area and sparse forest area (©ESA/JAXA – PALSAR)

Over **agriculture area** (Fig. 11 — Agri-area-2), the bluish crops exhibits surface scattering (S) with very low H, α -points to isotropic surface, and p_i are showing significance of only one scattering mechanism. Whilst the magenta cropland exhibits very high Anisotropy (ab. 0.84) where α — shows values ab. 30 deg which trends to isotropic dipole; the p_1 shows one major scattering mechanism. **Sparse forest** follow same dependencies observed over forests in spite of the third scattering mechanism is less important (p_3). The **urban areas** exhibits small entropy which is improper interpretation possibly due to the higher averaging.

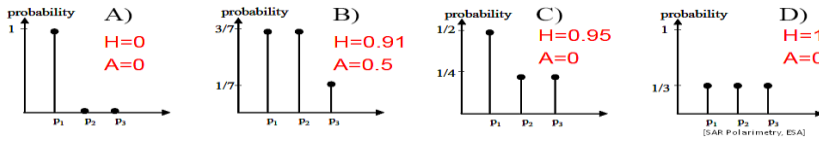


Fig. 12. Contribution of scattering mechanisms to the backscatter based on probabilities, depicted from Entropy (H) and Anisotropy (A) [10]

From the stated above it is clear that p_i , H and A control the number of scattering mechanisms (Fig. 12). To account for their contribution and thus to relate them to the physics of the scattering media, combinations of H and A are considered:

- A) Only one mechanism, when $H = 0$, $A = 0$: $(1-H)(1-A)$
- B) Two major equal mechanisms, when $H > 0.9$, $A > 0.5$: (HA)
- C) Two mechanisms unequally strong, when $H > 0.9$, $A = 0$: $(1-H)A$
- D) Three mechanisms equally strong, when $H = 1$, $A = 0$: $H(1-A)$

Hereupon, the first dependency — **A**) contributes to the analysis stated above at Scene-3 over the mountainous hilly area (near peak “Mijur”, see Fig. 13 — top), proving the availability of only one scattering mechanism over the bluish strip (S). Whilst, at neighboring reddish strip, the second dependency — **B**) proves the availability of two major scattering mechanisms, which leads to *isotropic dipoles*.

Forests areas exhibit three equal scattering mechanisms, according to dependency — **D**) where entropy is showing complete randomness of the scattering media.

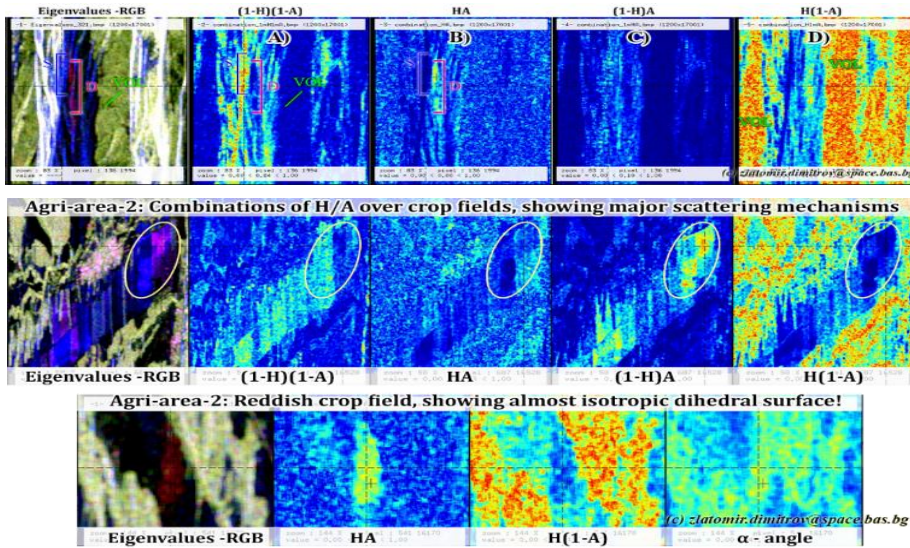


Fig. 13. On Scene-3 — Top: Mountainous area near peak “Mijur”—reddish stripe that exhibits dihedral surrounding isotropic surfaces in bluish; middle: Agri-area-2, crop fields with diversity of H/A; bottom: Reddish crops having pure dihedral (©ESA/JAXA – PALSAR)

Considering bottom of Scene-3 (Agri-area-2), whole H/A — combinations are observed where the magenta colored crops on Eigenvalues-RGB are kind of *anisotropic surface* with two mechanisms unequally strong (Fig. 13 — middle). A neighboring agri-field colored in pure-reddish on Eigenvalues-RGB (see Fig. 13 — bottom) should be an *isotropic dihedral surface* (with $\alpha \approx 90^\circ$ [10]), showing high consistency with — **B**). Despite, the α -angle is ab. 45 deg, therefore it points to — pure volume scattering constructed from oriented dipoles [8, 10].

Shannon Entropy and Radar Indices from Eigen-based decomposition

Measuring the degree of randomness according to the degree of depolarization is also part of the mathematical model of Eigenbased-decomposition where the eigenvalues set of parameters allows the following formulations [8]:

(16) Shannon Entropy (**SE**): **I** – intensity, **P** – polarimetric phase contribution :

$$SE = SE_I \{Tr[T_3]\} + SE_p \left\{ \frac{Det(T_3)}{Tr[T_3]} \right\}$$

(17) Radar Vegetation Index (**RVI**): $RVI = \frac{4\lambda_3}{(\lambda_1 + \lambda_2 + \lambda_3)}, RVI \in (0, \frac{4}{3})$

(18) Pedestal Height (**PH**): $PH = \frac{\min(\lambda_1, \lambda_2, \lambda_3)}{\max(\lambda_1, \lambda_2, \lambda_3)} = \frac{\lambda_3}{\lambda_1}, PD \in (0, 1)$

Shannon Entropy accounts about the randomization within scattering media by its intensity and polarimetric contribution term; RVI — accounts for the

homogeneity in the orientation of the canonical objects; PD — accounts for the strength of backscattered power of the non-polarized signal [8]. Another SAR indices exists in addition and show the de-polarization within the scattering media, such as — *Polarization fraction* and *Perplexity*. Consistency of those indices depends on the wavelength, and full polarimetry to be provided. **Important:** polarimetric descriptors derived from H-A- α theorem are roll-invariant — they doesn't rely on the rotation of the polarization ellipse around RLOS.

Shannon entropy normalized fractions — SE_I and SE_P — are showing particular sensitivity to the type and geometry of scattering media. Besides, high values on SE_I well delineate coherent targets (like — build-up areas) but also foreshortenings.



Fig. 14. Shannon Entropy — Intensity and Phase components, showing correlation with — build-up area (left), with foreshortening and forest density (right) (©ESA/JAXA – PALSAR)

It is observed that SE_I varies with the forest density, with values < 0.45 where changes relates also with variations in SPAN (see Fig. 14). Contrariwise, the polarimetric contribution term (e.g. Phase) is related to the degree of polarization, and shows high values — e.g. *random oriented dipoles* in forest [10]. The SE_P shows no-sensitivity on geometric distortions. Indication of depolarization due to anisotropic surfaces is showed over the *Perplexity index*, which correlates with — SE_P . The *Pedestal Height (PH)* index shows high degree of depolarization — $PH < 0.5$.

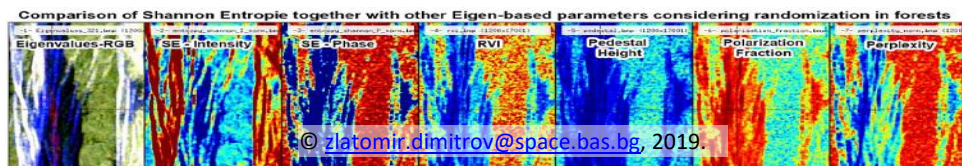


Fig. 15. Comparison of Shannon Entropy (SE_I and SE_P) with other SAR indices — RVI, PH, Polarization Fraction, and Perplexity accounting for depolarization in natural media

Over Agricultural areas same dependencies are observed where the isotropic surfaces (with one/two major scattering mechanisms — bluish from the Eigenvalues — RGB) are having highest — SE_I , and *Polarization fraction*, and lowest — SE_P , RVI and *Perplexity index*. Considering RVI, over each forest type it shows high values — $RVI > 0.45$ (Fig. 16).

A **comparison between Shannon Entropy** — SE, and Neuman’s Entropy — H — over *isotropic Bragg surfaces* (e.g. agricultural fields in bluish at Eigenvalues — RGB), H is very low contrary to the highest SE_I . Nonetheless, over such areas the H and SE_I have same texture patterns in between. Over forest SE_P have consistency with H, due to complete randomization. Could be concluded that, both entropies Neumann and Shannon — are not equal, but consistency in between is found due to physical meaning, when considering the both SE_I and SE_P .

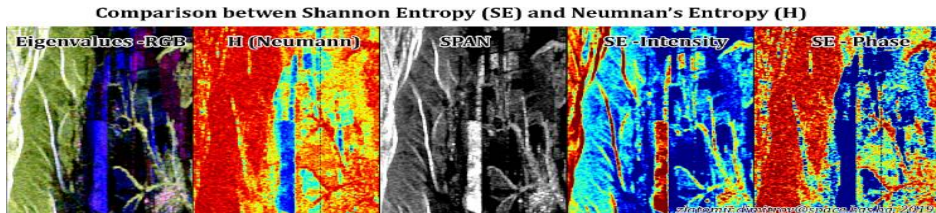


Fig. 16. Comparison, between Neumann's Entropy (H) and Shannon Entropy (SE — SE_I and SE_P); SE_I relate its changes with SPAN; SE — complements with H (©ESA/JAXA — PALSAR)

Model-based incoherent decompositions

Model based decompositions describe well polarimetric measurements from natural scatterers. Scattering models considers intrinsic properties of the canonical scattering mechanisms — e.g. Dipole (by means of its orientation), Bragg, Dihedral, Sphere, and Helix.

Yamaguchi-3 — component polarimetric decomposition — via $[T_3]$:

The Yamaguchi-3 (three) component scattering model relates polarimetric SAR measurements with three general orthogonal scattering mechanisms, imposing reflection symmetry conditions with scattering powers — P_S , P_D , P_V [6], where:

- Bragg-scattering (odd-bounce) from rough surface — P_S (β, fS) ;
- Even-bounce (DB) scattering from orthogonal surfaces — P_D (α, fD);
- Volume-scattering from cloud of randomly oriented dipoles — P_V . (fV);

Yamaguchi proposed the probability distribution function, where to represent more uniformly oriented dipoles (oriented along RLOS, on angle ψ [8]), which is more consistent with the backscatter from the natural scattering media, and better describe the volume scattering [6].

Analysis via the three powers — P_S , P_D , and P_V show better representation of the scattering mechanisms over forest areas and agriculture, where constructed RGB correlates well with the Eigenvalues-RGB and Pauli-RGB on Scene-3. As seen from Yamaguchi-RGB in comparison with Eigenvalues-RGB (Fig. 17), the particular colors representing scattering mechanisms are more distinguishable and saturated.

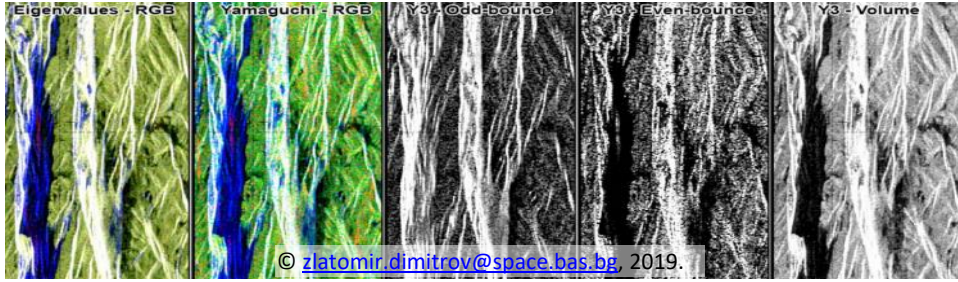


Fig. 17. Mountainous area near peak "Mijur": Yamaguchi's three-component incoherent Polarimetric Decomposition, based on physical scattering model, by — Odd and Even Bounce, and Volume (©ESA/JAXA – PALSAR)

Clear example is that within the forests are recognizable reddish patches with certain dihedral scattering, where $P_D \approx 2*(P_S, P_V)$, which is mostly consistent with vertical oriented dipoles (e.g. tree trunks). Moreover, the analysis over agricultural areas showed better recognition of the DB with values ab. -11 dB that is unlike via the Eigenbased — decomposition parameters (descriptors).

Freeman-2 — component polarimetric decomposition — via [C₃]:

The Freeman-2 (two) component polarimetric decomposition scattering model is initially intended to depict solely volume scattering from forest areas [5, 10]. Thus, selected contributing scattering mechanisms are only two, where:

- *First scattering mechanism:* volume scattering, contributed from random volume of dipoles with reflection symmetry;
- *Second scattering mechanism:* ground scattering contributed either — from dihedral from surfaces with different dielectric constants (e.g. DB from ground-trunk), or from Bragg-scattering of rough surfaces.

Hence, the second order statistics represented from Covariance matrix, is:

$$(19) [C_3] = C_{3G} + C_{3V}$$

Therefore, two power contributors of the total backscattered power are defined:

$$(20) SPAN = P_G + P_V, \text{ where: } P_G = P_G(f_G, \alpha), P_V = P_G(f_V, \rho), \quad \alpha, \rho \in \mathbb{C}$$

Here, α — controls the type of backscatter (i.e. Bragg or DB) and is sensitive to the forest density, whereas the ρ — is sensitive to the type of randomly oriented dipoles.

At scene-3, this two-component decomposition is showing in general poor discrimination between areas with one or two major scattering mechanisms. Nevertheless, over agricultural areas good discrimination is made of isotropic surfaces, where the strongest power in the ground contribution P_G is from Bragg-scatter, with values ab. -3 dB. Urban areas are well delineated with values ab. -6 dB.

In spite, good consistency of the volume contribution P_V is found over forest areas with values ab. -5.5 dB, but over sparse forest it could drop up to -9.8 dB (Fig. 4).

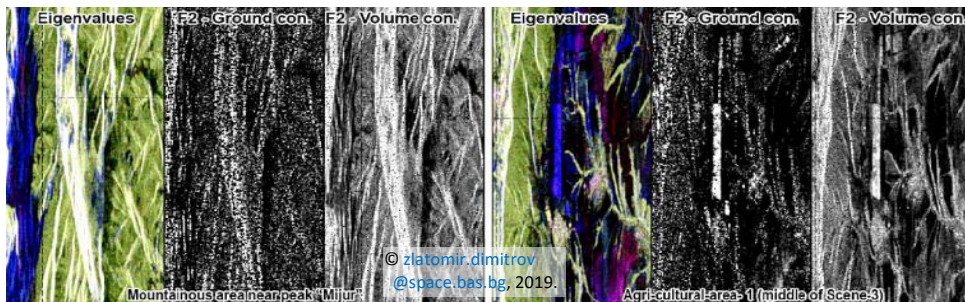


Fig. 18. Preview of Freeman-2 component physical polarimetric scattering model, over hilly mountainous location and agricultural fields, relating ground and volume contribution to the physics of the scattering process (©ESA/JAXA – PALSAR)

Comparison of polarimetric descriptors in two different acquisitions

A comparative analysis is made of whole polarimetric descriptors derived from Scene-1 and Scene-2 over same geographic area, with different seasonality.

Comparison between H/A/ α decomposition components (descriptors)

Comparative analysis considers the Eigen-based derived polarimetric descriptors — Eigenvalues-RGB, H, A, α -angle, RVI and PH. First comparison includes the interesting difference observed on decomposition parameters, over the **standing water body** located on bottom of both scenes. Due to intense raining, the eigenvalue — λ_1 (blue) is showing kind of a Bragg-backscatter, whereas H is very low; A — points out significance of the second and third scattering mechanisms, in spite α -confirms isotropic Bragg-surface. Completely the opposite is situation on Scene-1 (spring acquisition, calm weather) where, H — shows highest degree of randomness, maybe due to wind on that area, A — is meaningful, α — points out to anisotropic dihedral surface, with values > 45 deg (Fig. 19 — top).

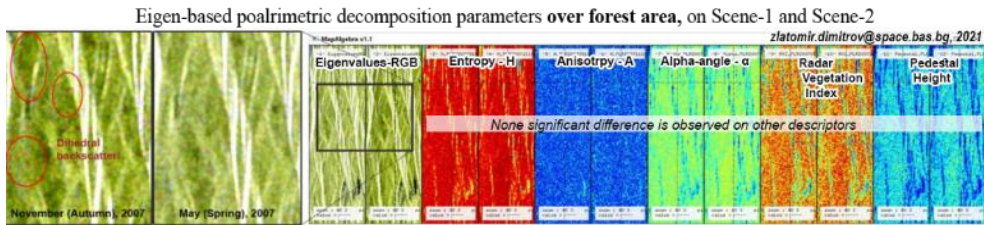
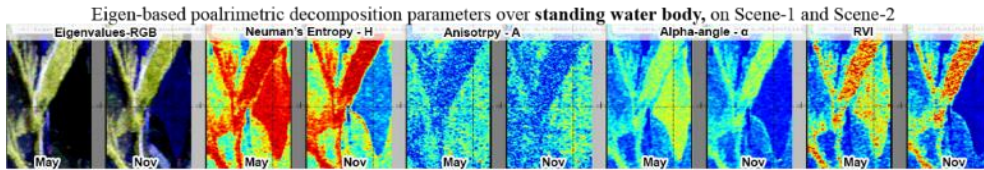


Fig. 19. Comparison of the Eigen-based decomposition, of scene-1 and scene-2 — top: example on Lake; bottom: example on forest area. At the November acquisition due to higher penetration a Dihedral backscatter is more recognizable. (©ESA/JAXA – PALSAR)

At the comparison over **forest areas**, the Eigenvalues-RGB on late autumn image (Scene-2) show distinct lower backscatter, rather than the spring one (Scene-1). Due to the higher penetration within the forest volume on Scene-2, particular reddish pixels are recognizable that suggests dihedral backscatter — i.e. from trunks. The rest of the parameters represent already observed high degree of randomness. Small increase in values is observed at autumn image (Scene2) on — α , RVI and PH, without distinct difference. Solely on RVI visible change is recognizable in forest.

Most of the difference between polarimetric descriptors are namely at the **agricultural areas**. On spring acquisition (Scene-1) uncultivated fields (pastures) caused low values in Eigenvalues, thus is black. Entropy is much higher, whilst Anisotropy suggests contribution from second and third scattering mechanisms.

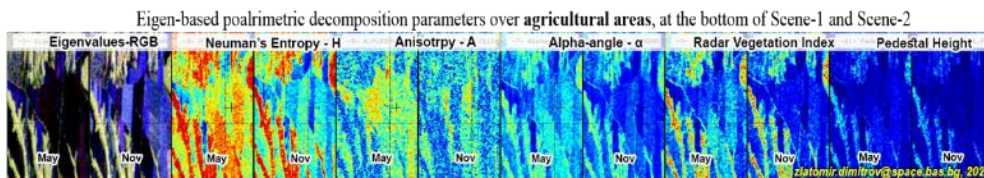


Fig. 20. Comparison of the Eigen-based decomposition, of scene-1 and scene-2: example on crop lands (©ESA/JAXA – PALSAR)

In spite, on autumn's acquisition (Scene-2), most of the fields have been already planted with winter crops that have already sprouted. Transition of high Entropy values to lower ones is observed here, along change of the physical properties of the scattering media that is observed also at A, α -angle and RVI. Interestingly, the Pedestal Height over this area is less affected and stays quasi constant.

Comparison between Freeman-2 decomposition components

The comparison between Freeman2 decomposition parameters gives another point of view that complement to the above analysis, by emphasizing on forest areas.

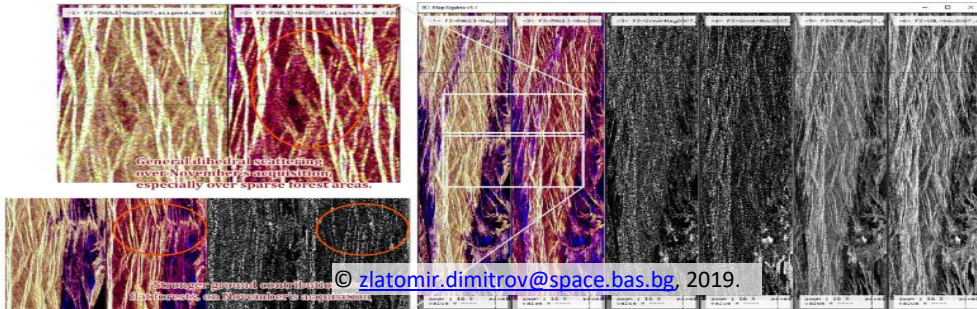


Fig. 21. Comparison between Freeman-2-decomposition, scenes — Scene 1- May, 2007 (first column) and Scene 2 — November, 2007 (second column). Example over forest areas showing leaf-off period, and increased dihedral scattering and ground contribution.

(©ESA/JAXA – PALSAR)

It is obvious the reduced volume backscatter contribution from the forest areas, observed at November's acquisition (Scene-2) — see Fig. 21. Comparing the pseudo-Pauli-RGBs, the November's image is darker, due to higher ground contribution to the total backscatter, due to leaf-off period in forest. Thus, general dihedral scattering is observed on Scene-2, especially over sparse forest areas. In flat forest, manmade objects are recognizable, in respect to May's image (Scene-1). Interesting fact is that the foreshortening strips from the November's acquisition are brighter, rather than May's acquisition. In spite of that, Scene-2 ground contribution gives better representation of the urban areas, due to fade out of vegetation at the resolution cell. Whereas the largest heterogeneity in backscatter is observed over agricultural areas. Ground contribution is far higher on November's image, rather than May's acquisition, due to phenological crop status for this period.

Polarimetric segmentations and classifications

Polarimetric segmentations are part from POL-SAR classifications, which sample polarimetric data by distribution algorithm (e.g. Wishart) of the second order statistics — $[T_3]$ and $[C_3]$ [8, 11]. Number of classes are determined from polarimetric data, but mostly they constitutes of 8 or 16 — classes, from Wishart distribution.

Polarimetric segmentation in H-A and H-A- α panes:

Firstly, the H- α plane is analyzed, which shows importance of the classes — 2, 3, 5, 6, 7 and 8, over Scene-3. General polarimetric segmentation into 8 — real classes is presented on Table-4. Refer to that according also to the segmentation applied in Fig. 22 — left, interpretation shows that most occurrences are in vegetation class (5). At the surface roughness propagation class (8), isotropic Bragg

surfaces have less occurrences having more anisotropic character. The branch/crown structure class (3) shows most occurrences resulted from correlation between H and α . The cloud isotropic needles classes (6) follows up, probably due to large scale forest areas whole over the scene, consisted of randomly oriented dipoles. Class (2) also comprises isotropic dihedral backscatter from forest.

Table 4. The H/ α — segmentation plane classes, of major scattering mechanisms from polarimetric data, which breaks into 8-regions (classes) with enumeration [11]

1	Dihedral scatterer	4	Dipole	7	Bragg Surface
2	Forestry DB	5	Vegetation	8	Surface Roughness propagation effects
3	Branch / Crown structure	6	Cloud of Anisotropic Needles	9	No feasible region

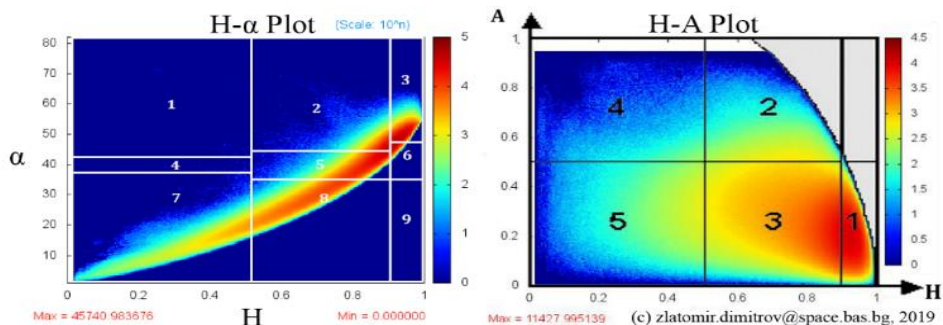


Fig. 22. Left: H- α segmentation plot (segmentation plane), showing frequency distribution in respect to the type of the scattering media; Right: The H-A segmentation plane for Scene-3, showing the character of the scattering media (surface)

Further analysis concerns the H-A segmentation plane, which is another approach for representing physical properties of the scattering media in respect to the type of backscatter. As seen from Fig. 22 — right, and Table-5, classes are:

Table 5. Th H/A — segmentation plane classes, with contribution mainly from least significant scattering mechanisms [8]

1	Random scatterers	3	Random surfaces	5	Bragg surfaces
2	Random anisotropic scatterers	4	Two scattering mechanisms	[Jagdhuber, T., GEO414]	

From the H-A plane presented above calculated for Scene-3, could be stated that in general the scattering media is constituted by random scatterers (class-1) and the random surfaces (class-3), which are in the sake of large scale forest areas, mixed

up with agricultures. Bragg surfaces have less occurrences in class-4, related with bare fields, and some particular crops on Scene-3 (see Eigen-based decomposition).

Concurrent classifications using classes from the segmentation panes are applied. The $H-A-\alpha$ classification shows most distinct separation between classes. Forests as random scatterers are well delineated (electric bluish, Fig.23), which is thus so also on $H-A$, and $A-\alpha$ (light-green and dark-green colors). Bragg surfaces in $H-A-\alpha$ are colored in pure red color, whilst anisotropic surfaces are well recognized. Scattering delineation at $H-\alpha$ classification is based on α -angle, thus Bragg surfaces are more distinct here (dark-blue), whilst the rest is mixed up. The $H-A$ shows different delineation due to Anisotropy. The anisotropic surfaces (magenta colored fields at Eigenvalues- RGB) are well classified at the $H-A$ and $A-\alpha$ classifications.

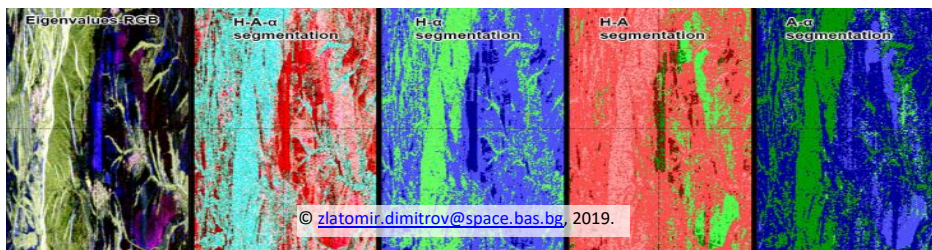


Fig. 23. Comparison of — form left to right: Eigenvalues- RGB , $H-A-\alpha$, $H-\alpha$, $H-A$, and $A-\alpha$ classifications over particular segmentation, on agricultural area -2 with surrounding forest areas, located at the bottom of Scene-3 (©ESA/JAXA – PALSAR)

Polarimetric Classifications using Wishart classifier:

In purpose of the analysis, the following unsupervised Wishart classifications are calculated [11]:

- $H-\alpha$ Wishart — composited of 8-stable clusters (classes)
- $H-A-\alpha$ Wishart — composited of 16 stable clusters (classes), same prerequisites, but more comprehensive due to including information from Anisotropy.

Advantage of the $H-A-\alpha$ Wishart classification with 16-classes is the discrimination of the second and third scattering mechanisms. Anisotropy allows to split clusters to smaller ones, with more distinct separation in physical manner. Starting point of the analysis is classification based on Pauli- $Decomposition$, from the Wishart $H-\alpha$ or $H-A-\alpha$ classifiers. The Pauli's $H-\alpha$ classification improperly classifies dihedral scattering (e.g. urban areas). Good separation of anisotropic and Bragg surfaces is present at the Pauli $H-A-\alpha$ classification. As seen in Fig. 24, Wishart classifications are detailed, thus hardly is interpretation of resulted clusters, especially the 16-classes one. In spite, performance of the both classifications over forest areas is straightforward, where particular sensitivity is observed for the sparse

forest and deforested areas. The benefit from Anisotropy, which discriminates the second and third scattering mechanisms from is obvious, with a close look at mountainous area near “Peak Mijur”. Considering the already discussed reddish strip, which exhibits contribution of two equal major mechanisms, is well separated at the 16-classes classifications, whilst is not at the 8-classes one (Fig. 24 — top).

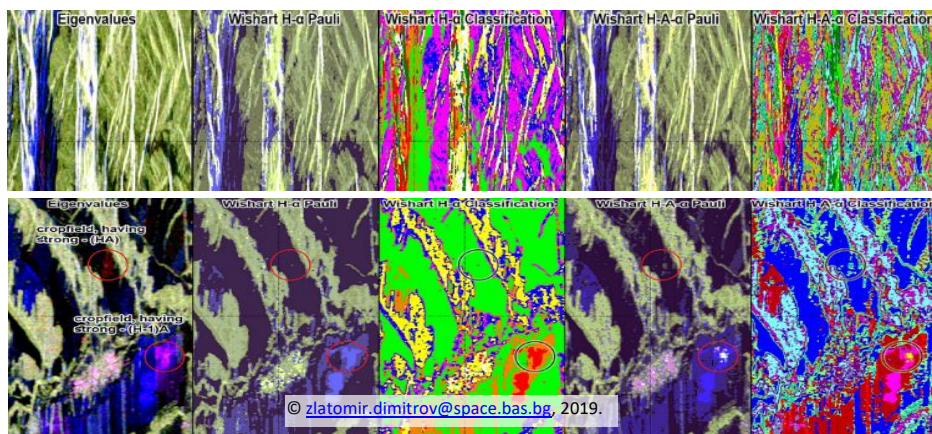


Fig. 24. Top: Comparison over mountainous area of peak “Mijur” on Scene-3 showing better performance of the H-A- α — 16-classes in regard to the 8-classes one; bottom: Crop fields near Agri-area-2 on Scene-3 having different physical origin of the backscatter (©ESA/JAXA – PALSAR)

The same is observed over agricultural areas (Fig. 24 — bottom), considering already discussed pure reddish crop on Eigenvalues (related to an isotropic dihedral surface that exhibits two equally strong scattering mechanisms), and magenta-one (related to an anisotropic dihedral surfaces with two unequally strong mechanisms).

Forest mask proposal, based on derived polarimetric descriptors

Forest is kind of a scattering media consisted of randomly oriented dipoles, inducing high degree of depolarization, with three equal scattering mechanisms at target vector. This leads to the general conclusion that most discriminative polarimetric descriptors should be such polarimetric parameters showing high degree of depolarization and randomization, such as — *RVI*, *Pedestal height*, *Perplexity*. In spite, in non-deterministic targets multiple scattering occurs, which induces phase differences, pointing out to different height of the phase centers. This was already observed on the phases of polarimetric coherences, and SE_p . Therefore, based on conducted polarimetric analysis of whole PALSAR scenes, the following discrimination of polarimetric descriptors **to delineate forest area**, could be done:

Table 6. Selected Polarimetric descriptors, which pixels represents the forests areas, and could be used to generate – **Forest/Non-forest Mask** (©ESA/JAXA – PALSAR)

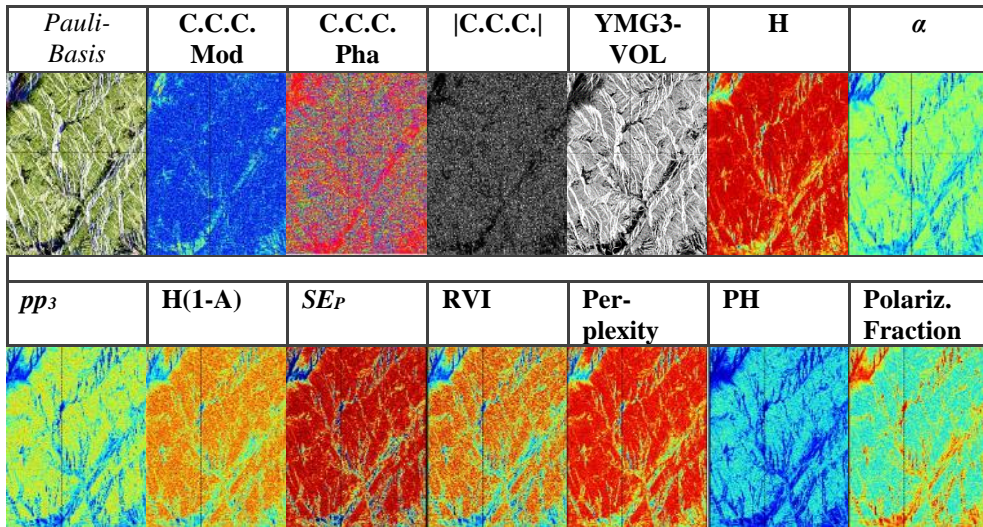


Table 7. Values and intervals of selected Polarimetric descriptors that delineates forest from non-forest pixels, derived from on-screen analysis, over whole PALSAR PLR scenes

Descriptor	Values / Interval	Descriptor	Values / Interval
C.C.C. Mod	< 0.42	H(1-A)	> 0.6
C.C.C. Pha	∈ -150 – 150 [deg]	SEP	> 0.88
 C.C.C. 	> 1.1 [dB]	RVI	> 0.7
YMG3-VOL	> -12 dB	Perplexity	> 2.5
H (Neumann)	> 0.8	PH	> 0.26
α-angle	∈ 38.0 -53.0 [deg]	Pol. Fract.	< 0.6
pp3	> 0.17		

Conclusion

General conclusion from the conducted polarimetric study is that POL-SAR provides extensive information about biophysical and geometrical properties of the scattering media. Natural targets like forest and agricultural areas are well described by the thorough analysis of incoherent Polarimetric decompositions. Resulting polarimetric descriptors are main tool for characterization of the scattering media.

Considering Speckle filtering in vegetation areas algorithms without edge preservation (e.g. BOXCAR) are reasonable to obey introducing artifacts. In spite, adaptive filtering with edge preservation (e.g. R. Lee) is important where certain geometry is present (e.g. in urban areas). In spite, the low modulus of Polarimetric coherences is due to presence of non-deterministic targets where complex scattering

persists. At those areas, higher phase differences points out different location of the active phase centers — i.e. scattering mechanisms.

From the Eigen-based mathematical decomposition theorem one could concluded that isotropic areas produce mostly surface scattering with general contribution of odd-bounce. Forest areas are related to random oriented dipoles ($\alpha \approx 45^\circ$) which gives complete randomness whilst anisotropic surfaces (e.g. agriculture) resulted with two scattering mechanisms with equal probabilities. Urban areas resulted with two unequal scattering mechanism, possibly due to averaging of non-deterministic (e.g. trees) with deterministic (e.g. buildings) targets. Combinations of H/A is of great benefit in analysis of agricultural areas where to relate the observed physics to the scattering media. From the Yamaguchi-3 component physical decomposition could be concluded that scattering mechanisms are well depicted within natural scattering media. The Freeman-2-component polarimetric decomposition is well utilized over forest areas and other natural media via its volume contribution. In spite, the ground contribution gives good results in the delineation of rough isotropic surfaces with Bragg-backscatter.

From comparison of two acquisitions, could be concluded that changes in the physics of the backscatter due to seasonality — like leaf-off in forests or other environmental conditions, could be fully analyzed by means of derived polarimetric descriptors. Prompt analysis of the phenology changes in crops is more suitable to be done by Eigen-based decomposition theorem and concurrent Radar indices.

Considering Polarimetric segmentation, most discriminative is the scattering derived from random surfaces. Good discrimination is achieved also over isotropic Bragg surfaces especially with propagation effects which also is related to non-deterministic targets. Problems in Wishart classification algorithms mainly concerns the misclassification of the pixels with equal characteristics aiming the edge value of the clusters. As observed, to the forest area five classes are dedicated from the 8-classes classification, whilst at the 16-classes one, the number of forest classes got doubled. Therefore, increasing number of classes by means of anisotropy leads to further maze and fragmentation of the land cover classes, especially over forest areas with varying density. Nevertheless, one could concluded that the isotropic and Bragg surfaces are well classified by both unsupervised Wishart classifications.

Finally, randomization in natural media could be exploited to derive Forest/Non-forest mask from polarimetric descriptors of full polarimetric SAR data.

Acknowledgment

I would like to sincere thank Dr. T. Jagdhuber for supporting my interest in Polarimetry during the course GEO414 that resulted in writing this paper. Wish to thank also Prof. C. Schmullius, *Lehrstuhl für Fernerkundung*, for the giving me this precious opportunity to take part at the Courses of MSc in Geoinformatics, at FSU-Jena, in the framework of the ERASMUS+ program. Wish also to thank my

tutor in Bulgaria Prof. E. Roumenina for supporting me during my PhD. I acknowledge also to ESA and JAXA for providing me with PALSAR PLR data.

References

1. Le Toan, T., S. Quegan, M.W.J. Davidson, *et al.* The BIOMASS mission: Mapping global forest biomass to better understand the terrestrial carbon cycle. *Remote Sensing of Environment*, 115, 2011, 2850–2860, DOI:10.1016/j.rse.2011.03.020.
2. Ainsworth, T. L., J. P. Kelly, J.-S. Lee. Classification Comparisons Between Dual-Pol and Quad-Pol SAR Imagery. *Proceedings of ISPRS Journal of Photogrammetry and Remote Sensing*, 64, 2009, 464–471.
3. Rosenqvist, A., M. Shimada, N. Ito, M. Watanabe. ALOS PALSAR: A pathfinder mission for global-scale monitoring of the environment. *IEEE TRANSACTIONS ON GEOSCIENCE AND REMOTE SENSING*, 45, 2007, 3307–3316.
4. Erxue, C., L. Zengyuan, T. Xin, F. Fengyun. FOREST STRUCTURE INFORMATION EXTRACTION FROM POLARIMETRIC ALOS PALSAR DATA. *PI No. 315. Institute of Forest Resources Information Technique, CAF*, 2009, 6 p.
5. Cloude, S. R., E. Pottier. A Review of Target Decomposition Theorems in Radar Polarimetry. *IEEE Trans. Geoscience and Remote Sensing*, vol. 34, 1996, 498–518.
6. Yamaguchi, Y., S. Akinobu, R. Sato, H. Yamada, J. Yang. A New Four-component Scattering Power Decomposition Applied to ALOS-PALSAR PLR Data Sets. Niiigata University, Japan, 2010, 4p.
7. Jagdhuber, T. An Approach to Extended Fresnel Scattering for Modeling of Depolarizing Soil-Trunk Double-Bounce Scattering. *MDPI, Remote Sens.*, 8, 818, 2016, 25 p. doi:10.3390/rs8100818.
8. Jagdhuber, T., C. Schmillius. SAR Polarimetry — Theory and Applications. *Lecture and Exercise (Course materials with closed access), GEO-414 Masterkurs*, Friedrich-Schiller-Universität-JENA, 2019, 305 p.
9. López-Martínez, C, L. Ferro-Famil, E. Pottier. 3. SPECKLE FILTERING. *PolSARPro Tutorials*, Part-I, Chapter-3, ESA, 2005, 12 p.
10. López-Martínez, C, L. Ferro-Famil, E. Pottier. 4. POLARIMETRIC DECOMPOSITIONS. *PolSARPro Tutorials*, Part-I, Chapter-4, ESA, 2005, 28 p.
11. López-Martínez, C, L. Ferro-Famil, E. Pottier. 5. POLARIMETRIC SAR DATA CLASSIFICATION. *PolSARPro Tutorials*, Part-I, Chapter-5, ESA, 2005, 14 p.

ИЗПОЛЗВАНЕ НА ПОЛЯРИМЕТРИЯ (POL-SAR) НА ТЕСТОВИ РАЙОНИ В СЕВЕРОЗАПАДНА БЪЛГАРИЯ – ПОЛЯРИМЕТРИЧНИ ДЕСКРИПТОРИ, ДЕКОМПОЗИЦИИ И КЛАСИФИКАЦИИ

З. Димитров

Резюме

Статията представя приложение на Поляриметрия (POL-SAR) в планински и равнинен тестови райони в Северозападна България, с изображения в пълна поляриметрия от спътниковата система в микровълнов канал – L – ALOS1 PALSAR на Японската космическа агенция (JAXA). Приложени са всички основни методи в поляриметрията, като са изчислени множество поляриметрични дескриптори, като резултат от поляриметрични декомпозиции и поляриметрични кохерентности. Анализирано е поведението на поляриметричните параметри при различни видове разсейващи обекти, свързвайки механизмите на разсейване с вида на разсейващата среда. Направено е сравнение в планински горски територии от две дати на заснемане – май (през пролетта) и ноември (през есента). Приложени са поляриметрични сегментации и класификации с 8 и 16 класа. Накрая е предложена маска на горската територия, на база на поляриметричните дескриптори. Статията е разработена по линия на положен Курс – GEO414, към обмен по програма ЕРАЗЪМ+ на ЕС в Университета в Йена, Германия. Докладът е представен на поредната Седемнадесета международна научна конференция „Космос, Екология, Сигурност (Space, Ecology, Safety) –SES 2021“.